Spatial-contrast analysis in a cold-atom Sagnac interferometer with a single large Raman beam

Tae Hyun Kim, Sin Hyuk Yim, Kyu Min Shim, and Sangkyung Lee
Agency for Defense Development, Daejoen 34186, Republic of Korea
(Received 5 December 2016; published 29 March 2017)

We have developed a cold atom Sagnac interferometer with a single large Raman beam. In combination with a time-of-flight measurement performed by thin probe beams, the variation in spatial contrast of the atomic Mach-Zehnder interference was analyzed by considering the spatial intensity profile of the single large Raman beam and the spatial density profile of the atomic cloud. Based on our analysis, we determined that contrast enhancement is attainable using the spatial selection of the atomic cloud but it reduces angular velocity sensitivity.

DOI: 10.1103/PhysRevA.95.033632

I. INTRODUCTION

Light-pulse atom interferometers provide a precise way of measuring physical constants [1–3], gravity [4–6], and rotation [7–11]. Certain types of light-pulse atom interferometers, where stimulated Raman transitions serve as an atomic wave packet splitter, have been widely developed, especially for measuring gravitational acceleration and rotation. In order to measure the acceleration of gravity, only a single Raman beam propagating along the vertical direction is required. For rotation sensing, however, three spatially separated Raman beams are usually required to achieve the long interrogation time [7,9]. Those three individual Raman beam optics, however, have alignment and maintenance issues [7]. On the other hand, a single Raman beam configuration is easy to align, is free from the unwanted phase shifts caused by alignment of the three Raman beams, and can have a good long-term stability. For rotation sensing, large single Raman beam optics can be used in cases where high sensitivity is not required, because the beam size limits the interrogation time, which is critical to sensitivity. Recently, three narrow slits in a large single Raman beam were applied to a low-velocity intense source (LVIS) based light-pulse atom interferometer [12]. A single large Raman beam type cold-atom Sagnac interferometer based on moving molasses was also studied [11,13]. It is well known that the contrast in an interference fringe is limited by the inhomogeneous Rabi frequencies originating from the Raman laser intensity profile. But a detailed analysis of the spatial variation in spatial contrast has not yet been studied. The inhomogeneous Rabi frequencies arising from the Raman beam intensity profile are remarkable in such cold-atom Sagnac interferometers because the atomic cloud is crossing the Raman beam along the radial direction, while in gravimeter-type interferometers the atomic cloud is moving along the axial direction.

In this paper we observed and analyzed the atomic Mach-Zehnder interference induced by a single large Raman beam with the help of a time-of-flight measurement, based on thin probe beams, whose widths are 3.8 times smaller than the size of the atomic cloud. The variation in spatial contrast in the atomic cloud was analyzed by considering the spatial intensity profile of the single large Raman beam and the atomic density profile. Based on our analysis, we found that the spatial selection increases contrast, but it degrades the angular velocity sensitivity.

II. EXPERIMENTAL SETUP

Figure 1(a) shows the schematic diagram of the experimental setup. Rubidium 87 atoms are trapped and cooled by a typical magneto-optical trap for 698 ms of the loading time in the MOT chamber. Atomic clouds are launched at an angle of 12 deg with respect to the horizontal plane during a moving molasses stage of 2 ms. The following 2 ms polarization gradient cooling stage reduces the temperature of the atomic clouds to 3.67(0.9) μK, which is measured by Raman velocimetry [14]. The mean speed of the atomic clouds is 3.34 m/s along the y axis (longitudinal direction). The manipulation and detection of the atomic wave packet is performed in a glass chamber (40 mm $\times$ 40 mm $\times$ 140 mm). Two slightly angled bias coils outside the glass chamber generate a bias magnetic field of 0.96 G to define the quantum axis.

In a state-preparation stage, both the Zeeman optical pumping laser, which is resonant on the $F = 2 \rightarrow F' = 2$ transition, and the repumping laser simultaneously illuminate the atomic cloud to prepare atoms in the $F = 2, m_F = 0$ state. The polarization of the Zeeman optical pumping beam is parallel to the bias magnetic field, π-pol. During the preparation stage, the atomic cloud is heated to a temperature of 5.46(0.7) μK [9].

After a preparation stage, three pulses in a large single Raman beam of 25 mm $1/e^2$ radius separate, reflect, and recombine the cold atomic wave packets, as shown in Fig. 1(b). The attainable interrogation time in our Raman beam optics is about 3.75–4 ms. The direction of the Raman beam propagation is perpendicular to gravity, as shown in Fig. 1(a). Each of the Raman pulses has a pulse duration of 5 μs, which is achieved by using an optical switch consisting of an 80 MHz acousto-optic modulator (3080-1, Crystal tech.), an RF switch (ZSDR-203+, Mini-Circuits), and a digital pulse generator (DG535, SRS). The shorter Raman pulse enhances the Raman transition efficiency because the velocity linewidth of the Raman transition covers more of the atomic velocity distribution [13]. The optical common detuning Δ of the Raman beams is -1 GHz detuned with respect to the cooling transition. The Raman beam intensity ratio of Raman stokes to Raman pump is adjusted to 0.5 which minimizes the ac stark shift. The Raman detuning δ, which is the frequency difference between the Raman stokes and the Raman pump beam, is adjusted by using an arbitrary function generator

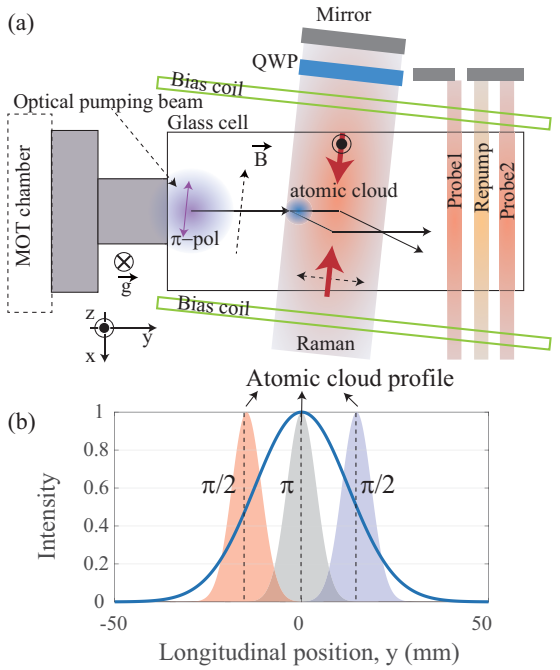

FIG. 1. (a) Schematic diagram of the experimental setup. (b) Raman beam intensity profile (blue solid line) and density profile of atomic clouds (filled area) at the first $\pi/2$ (red), the second π (gray), and the third $\pi/2$ (blue) pulse positions. The $1/e^2$ radius of the Raman beam is 25 mm and the $1/e$ radius of the atomic cloud is 5.6 mm.

(AFG3101C, Tektronix). The details of our Raman system are given in Ref. [15]. To achieve sufficient optical power, the phase-locked Raman stokes and Raman pump beam are simultaneously injected into a tapered amplifier (BoosTA pro, Toptica). The maximum power of the two mode Raman beam is 700 mW after a fiber coupling.

In the interferometry stage, the phase of the third $\pi/2$ pulse is changed by an isosceles triangular frequency sweep that is composed of a $t_c = 1$ ms sweep time and a $t_c = 1$ ms return time. The resulting Raman laser induced phase difference is given by $\Delta\phi_{\text{laser}} = \beta t_c^2$, where β is the frequency sweeping rate.

We measured the atomic population as a function of the phase of the third $\pi/2$ Raman pulse. A $lin \perp lin$ Raman beam polarization configuration, where the incident Raman beam has a horizontal polarization and the retroreflected Raman beam passing through a quarter-wave plate has a vertical polarization, induces a constructive interference between the two stimulated Raman passages, $\sigma^+ - \sigma^+$ and $\sigma^- - \sigma^-$. This allows a nonzero k_{eff} which generates acceleration and a rotation-induced phase. In order to select a splitted atoms's path by utilizing the Doppler shift, the Raman beam line is angled 84 deg to the atom's mean velocity.

After an atomic Mach-Zehnder pulse sequence, the resulting atomic populations in the $F = 2$ and the $F = 1$ state are detected by two time-of-flight measurements, for normalization of the atomic population. Two thin probe beams (1.45 mm × 20 mm), which are resonant on the $F = 2 \rightarrow F' = 3$ transition, induce fluorescence from the atoms in the $F = 2$ state. The width of the thin probe beams is 3.86 times smaller than the size of the atomic cloud, $\sigma = 5.6$ mm, in the detection region, so that it induces fluorescence from a slice of the atomic cloud which is comparable to the probe beam size, not the entire atomic cloud.

As a result, using this thin probe beam based time-of-flight measurement, we can extract spatial information along the longitudinal direction (y axis). The first probe is partially retroreflected in order to detect and blow out the $F = 2$ atoms. Between the two probes, the elongated repumping beam illuminates the atomic clouds to optically pump the $F = 1$ atoms to the $F = 2$ state. Therefore, fluorescence induced by the second retroreflected probe beam indicates the number of atoms in the $F = 1$ state. This normalization technique suppresses the effect of atomic number fluctuations in the atomic clouds on the signal-to-noise ratio. We can also determine the mean velocity of the atomic clouds by using the two time-of-flight signals. Each of the fluorescences is collected by a $f = 25$ mm lens pair and is sensed by a large area photodiode (Hamamatsu S1337-BR) with a transimpedance circuit.

III. RESULTS AND DISCUSSION

Figure 2(a) shows the measured velocity sensitive Raman spectrum. The large peaks shown at ±0.92 MHz come from the velocity sensitive Raman spectrum, and the small peak at zero detuning is the residual velocity insensitive Raman spectrum. The detuning of the large peak is determined by

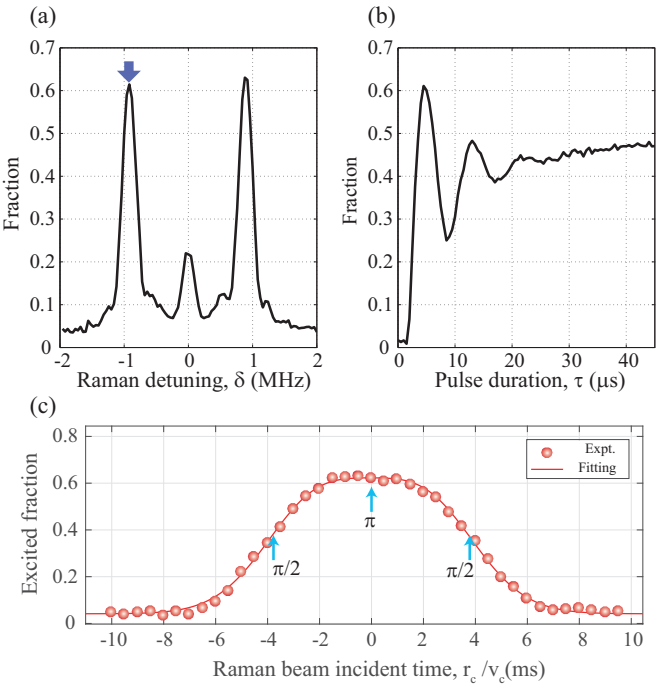

FIG. 2. (a) Velocity sensitive Raman spectrum as a function of Raman detuning δ. The blue arrow indicates the Raman detuning used in the experiment. (b) Velocity sensitive Rabi oscillation as a function of pulse duration τ at the fixed Raman power of 700 mW. (c) Fraction as a function of Raman pulse flashing timing. The red filled circles and the red solid line indicate the experimental data and fitting by Eq. (5), respectively.

$\delta_{\text{counter}} = |\vec{k}_{\text{eff}}||\vec{v}|\cos\theta$, where θ is the angle between the mean atomic velocity and the effective wave vector. In the case of Raman detuning of -0.92 MHz, the calculated θ is 86 deg. The FWHM of the velocity sensitive Raman spectrum is about 222 kHz, which covers the atomic velocity distribution at a temperature of 5.46 μK. The Raman detuning δ was fixed at -0.92 MHz.

Figure 2(b) shows the measured Rabi oscillation as a function of Raman pulse duration, which is used to find the pulse duration for the π pulse condition. The maximum excited fraction is shown at 5 μs, which is the π pulse condition at the total Raman beam power of 700 mW. As shown in Fig. 1(b), the $\pi/2$ pulse conditions are achieved by adjusting the Raman pulse incident timing with a fixed pulse duration. In other words, a pulsed Raman laser beam which is flashing when the atomic cloud is positioned at the half maximum intensity of the Raman beam realizes the $\pi/2$ condition. Figure 2(c) shows the excited fraction as a function of the time of the applied Raman pulse. The red solid line in Fig. 2(c) represents the fitted curve which describes the total excited fraction in the atomic cloud.

The total excited fraction results from the integration of the excited probabilities of individual atoms in the atomic cloud. It can be written as

$$S(\delta,\tau) = \int_{\vec{v}}\int_{\vec{r}} P(I(\vec{r}),\delta - \vec{k}_{\text{eff}}\cdot\vec{v},\tau)\rho(\vec{r},\vec{v})d^3r d^3v, \quad (1)$$

where $\vec{k}_{\text{eff}}$ is the effective wave vector of a counterpropagating Raman laser pair, $\vec{v}$ is the velocity of an atom, and δ is the Raman detuning, which is the frequency difference between two Raman laser modes. The atomic density function is given by $\rho(\vec{r},\vec{v}) = \rho_0(2\pi m k_B T)^{-3/2}(\pi\sigma^2)^{-3/2}\exp[-(\vec{r}-\vec{r}_c)^2/\sigma^2]\exp[-m(\vec{v}-\vec{v}_c)^2/2k_BT]$, where $\vec{r}_c$ is the position of the center of mass of the atomic cloud, σ is its $1/e$ radius, $\vec{v}_c$ is the velocity of the center of mass, and ρ_0 is the peak atomic density at the center of the atomic cloud.

Here we assume that the correlation between velocity and position in the atomic density function can be negligible because the spatial separation of atoms with differing momentum is comparable to the initial atomic cloud size, i.e., $|v - v_c|t_f \simeq \sigma_0$, where t_f is the atom's total flight time to reach the detection region and σ_0 is the initial atomic cloud size. In this regime atoms with differing momentum are not obviously resolved spatially, which means a weak position-velocity correlation. $P(I,\delta,\tau)$ is the excited probability of an atom, which is derived from the two level model:

$$P(I,\delta_{\text{eff}},\tau) = \frac{\Omega_{\text{eff}}^2}{\Omega_{\text{eff}}^2+\delta_{\text{eff}}^2}\sin^2\left(\frac{\sqrt{\Omega_{\text{eff}}^2+\delta_{\text{eff}}^2}}{2}\tau\right), \quad (2)$$

where δ_{eff} is an effective Raman detuning which contains a pure Raman detuning and a Doppler shift, and Ω_{eff} is the effective two-photon Rabi frequency which is proportional to the Raman beam intensity. The spatial intensity of the Raman beam I is given by $I(\vec{r}) = I_{\text{peak}}\exp(-2r^2/r_d^2)$, where I_{peak} is the peak intensity of the Raman beam and r_d is the $1/e^2$ diameter of the Raman beam, given by 25 mm in our experiment. In the experiment, the Raman detuning is set to compensate the Doppler shift $\delta_{\text{eff}} = \vec{k}_{\text{eff}}\cdot(\vec{v}_c - \vec{v})$. In the short Raman pulse duration regime, where the transit time broadening covers the Doppler broadening due to an atomic velocity distribution, we can expand Eq. (2) by the perturbation $\epsilon = |\vec{k}_{\text{eff}}\cdot(\vec{v}-\vec{v}_c)|/\Omega_{\text{eff}}$:

$$P \approx \sin^2\frac{\Omega_{\text{eff}}(I)\tau}{2} + O(\epsilon\cos\theta_k), \quad (3)$$

where θ_k is the angle between $\vec{k}_{\text{eff}}$ and $\vec{v}-\vec{v}_c$. When only the zero order term is taken, the velocity averaged atomic population can be written as

$$\int_v P d^3v \simeq \sin^2\frac{\Omega_{\text{eff}}(I)\tau}{2} + O(\xi^2), \quad (4)$$

where $\xi = \sqrt{\frac{2k_BT}{m}}(\frac{k_{\text{eff}}}{\Omega_{\text{eff}}})$. The first order term of $O(\xi)$ disappears after the velocity integration. In our experiment, $\xi \simeq 0.83$ at the temperature of 5.46 μK. In spite of the large perturbation parameter ξ where the higher order terms need to be considered, the experimental result is well fitted by just taking the zero order term.

Finally, position averaging is performed. In the large Raman beam regime where $r_d \gg \sigma$, given by $\zeta = \sigma/r_d = 0.22$ in our experiment, the resulting total excited fraction is approximated by

$$S \simeq \sin^2\left[\frac{\Omega_{\text{eff}}\tau}{2}\exp\left(-2\frac{r_c^2}{r_d^2}\right)\right] + O(\zeta^2). \quad (5)$$

As shown in Fig. 2(c), the experimental data are well fitted by Eq. (5). We can extract the beam radius $r_d = 25$ mm from the fitting. The distance between two $\pi/2$ pulses is given by $r_{\pi/2-\pi/2} = r_d\sqrt{2\ln 2}$ by Eq. (5). The total interrogation time $2T_R$ is easily obtained from the distance divided by the velocity of an atomic cloud, given by $2T_R = r_d\sqrt{2\ln 2}/v$. The deduced total interrogation time is trivial because a two-photon Raman Rabi frequency is proportional to the intensity of the Raman beam and the Raman beam intensity profile is described by a Gaussian function. In Fig. 2, the interrogation time is determined by $2T_R = 8$ ms, which is the time between the first $\pi/2$ pulse and the third $\pi/2$ pulse. A three Raman pulse sequence, $\pi/2$-π-$\pi/2$, realizes an atomic Mach-Zehnder interferometer which has an enclosed area. From the mean velocity of the atomic clouds (3.34 m/s) and the interrogation time of $2T_R = 8$ ms, the area of our interferometer can be calculated to be 0.62 mm^2.

The probability of an atom in the $F=1$ state or in the $F=2$ state can be written as $P_{F=1,F=2} = \frac{1}{2}[1 \mp \cos(\Delta\phi_{\text{laser}} + \Delta\phi_{\text{grav}} + \Delta\phi_{\text{rot}})]$, where $\Delta\phi_{\text{grav}} = \vec{k}_{\text{eff}}\cdot\vec{g}T_R^2$, which is the phase shift caused by gravitational acceleration, and $\Delta\phi_{\text{rot}} = -2\vec{k}_{\text{eff}}\cdot(\vec{\Omega}\times\vec{v})T_R^2$, which is a Sagnac phase term [16]. Here $\vec{v}_0$ is the initial mean velocity of the atomic cloud. The total fraction in the atomic cloud results from the space and velocity integration. Figure 3(a) shows the time-of-flight signals of the $F=1$ atoms and the $F=2$ atoms. It shows the π phase difference between the $F=1$ fraction and the $F=2$ fraction. Due to the existence of the weak position-velocity correlation, there is a position dependent Sagnac phase which causes the spatial interference [17]. But the spatial interference patterns are not observed because the Sagnac phase term originating from earth rotation, which is

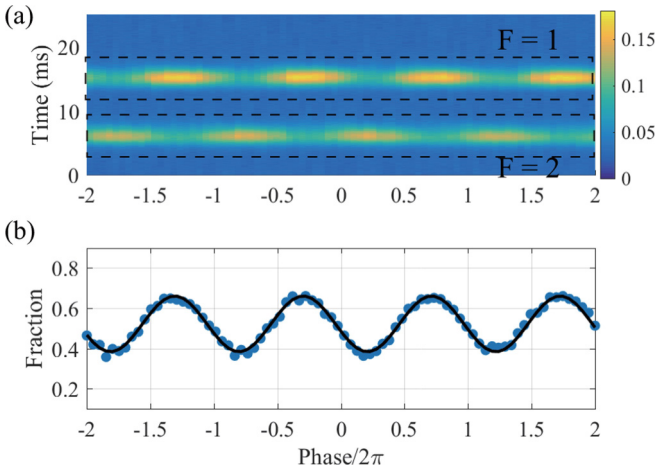

FIG. 3. (a) Time-of-flight signal as a function of the time and phase of the third Raman pulse. (b) $F = 1$ fraction as a function of the phase of the third Raman pulse. The time-of-flight signal is fully integrated. The blue filled circles indicate the experimental data and the black solid line depicts the sinusoidal fitting.

the only rotation source in our case, is too small. After full integration of the time-of-flight signals, we can obtain the interference fringe shown in Fig. 3(b). The black solid line in Fig. 3(b) is a fitting curve, $y = 1/2(1 - C\cos\Delta\phi)$.

The time-of-flight measurement performed by the thin probe beams provides the spatial information of the interference fringe. As shown in Fig. 1(b), the Raman beam has a spatial intensity profile, so that part of the atoms do not see the beam intensity of the $\pi/2$ or π pulse condition. This inhomogeneous pulse area induces a contrast drop. In order to model the contrast drop, we assume that the pulse area of the first (or third) Raman pulse is $\Omega_{R_1}\tau$ (or $\Omega_{R_3}\tau$) and the pulse area of the second Raman pulse is π since the atoms at the position of the $\pi/2$ pulse conditions experience a steeper intensity change than those at the position of the π pulse condition. The intensity gradients are given by 0 at the center of the Raman beam and $(-\sqrt{2\ln 2}/r_d)\hat{r}$ at the half maximum of the Raman beam intensity profile. After a $\Omega_{R_1}\tau$-π-$\Omega_{R_3}\tau$ pulse sequence, the probability of an atom in the $F = 1$ state can be written as

$$P_{F=1} = \tfrac{1}{2}\big[1 + \cos\left(\Omega_{R_1}\tau\right)\cos\left(\Omega_{R_3}\tau\right) - \sin\left(\Omega_{R_1}\tau\right)\sin\left(\Omega_{R_3}\tau\right)\cos(\Delta\phi)\big] + O(\epsilon\cos\theta_k), \tag{6}$$

where $\Delta\phi = \Delta\phi_{\text{laser}} + \Delta\phi_{\text{acc}} + \Delta\phi_{\text{rot}}$. Here we take the zero order term. From Eq. (6) and its velocity averaging, the contrast can be written as

$$C = \sin\left(\Omega_{R_1}\tau\right)\sin\left(\Omega_{R_3}\tau\right) + O(\xi^2), \tag{7}$$

where Ω_{R_1} and Ω_{R_3} are the Rabi frequencies of the first $\pi/2$ pulse and of the third $\pi/2$ pulse. τ is the pulse duration. Because a large Raman beam has a symmetric Gaussian intensity profile, the pulse area around the first (or the second) $\pi/2$ pulse condition is approximated by $\frac{\pi}{2}(1 \mp \frac{\Delta r}{r_d}2\sqrt{2\ln 2})$ where Δr is the distance of an atomic cloud slice from the center of the atomic cloud. The Pulse area can be rewritten as $\Omega_{R_1}\tau = \frac{\pi}{2} + \eta$ and $\Omega_{R_3}\tau = \frac{\pi}{2} - \eta$. Here η is a pulse area

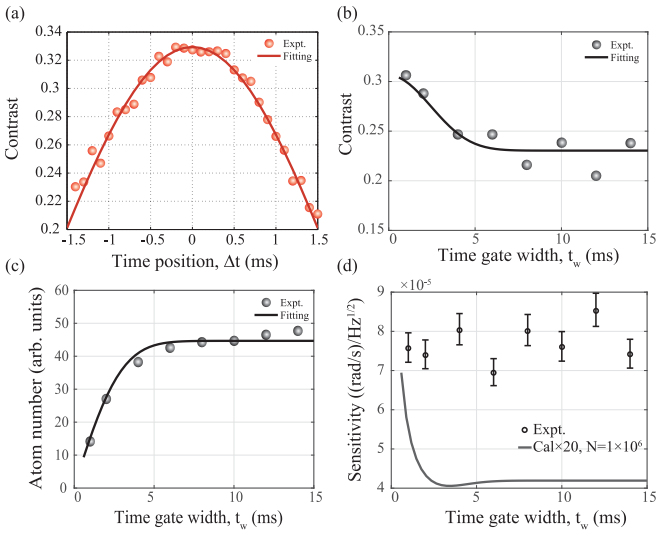

FIG. 4. (a) Contrast as a function of position of an atomic cloud slice. The red circles and red solid line depict the experimental result and fitting, respectively. (b) Contrast as a function of the time gate width of an atomic cloud slice. (c) Atom number as a function of the time gate width of an atomic cloud slice. (d) Calculated and measured short-term sensitivities. We note that the calculated short-term sensitivity is magnified by 20.

perturbation given by $\eta = -\frac{\pi\Delta r}{r_d}\sqrt{2\ln 2}$. The approximated contrast is calculated by

$$C = \cos^2\left(\frac{\pi\Delta r}{r_d}\sqrt{2\ln 2}\right) + O(\xi^2). \tag{8}$$

Figure 4(a) shows the contrast as a function of 0.1 ms time gate positions. The red solid line indicates the fitted curve $y = A\cos^2(B\Delta t)$, where $A = 0.32937(\pm 0.00134)$ and $B = 449.4(\pm 9.56)$. The A parameter represents the maximum contrast of our system. It is limited by the Raman transition efficiency which is mainly affected by the atomic cloud velocity distribution and the thermal expansion of the atomic cloud. The Raman transition efficiency can be obtained by measuring the Rabi oscillation. As shown in Fig. 2(b), the Raman transition efficiency of the entire atomic cloud is 60%. Therefore, the averaged contrast C_{total} of the entire atomic cloud is roughly estimated as $0.6^3 = 0.22$. The relation between the averaged contrast of the entire atomic cloud and the maximum contrast A is written as $C_{\text{total}} = \frac{A}{2}[1 + \exp(-\frac{2\ln 2\pi^2\sigma^2}{r_d^2})]$, obtained from Eq. (9) in the limit $t_w \to \infty$. We can easily calculate the maximum contrast A as 0.3 by using the known parameters; the averaged contrast C_{total}, the size of the atomic cloud σ, and the size of the Raman beam r_d. It is very close to the fitted value 0.32937. The B parameter indicates the degree of the variation of the spatial contrast which relates to the gradient of the Raman beam intensity. From Eq. (8) and $\Delta r = v_c\Delta t$, the expected B is given by $B = \frac{\pi v_c}{r_d}\sqrt{2\ln 2}$. The Raman beam size ($r_d = 25$ mm) and the mean speed of the atomic clouds ($v_c = 3.34$ m/s) determine the B parameter as 494.2. The calculated B is close to the fitted value 449.4. The calculation including higher order $O(\xi^2)$ terms will give a more correct result.

We can obtain the maximum contrast by selecting the center of the atomic cloud. Additionally, the contrast is observed as a function of the temporal width of an atomic cloud slice. When the interference phase $\Delta\phi$ is independent of the atom's position, the averaged contrast in an atomic cloud slice can be written as

$$C(t_w) = \frac{\rho_0}{\sqrt{\pi}\sigma} \frac{\int_{-t_w/2}^{t_w/2} v_c A \cos^2\left(\frac{\pi v_c t \sqrt{2\ln 2}}{r_d}\right) \exp\left(-\frac{v_c^2 t^2}{\sigma^2}\right) dt}{N(t_w)}, \tag{9}$$

where t_w is the time gate width of an atomic cloud slice and $N(t_w)$ is the atom number in an atomic cloud slice, given by $N(t_w) = \rho_0(\pi\sigma^2)^{-1/2} \int_{-t_w/2}^{t_w/2} v_c \exp(-v_c^2 t^2/\sigma^2) dt$. This is depicted as the black solid line in Fig. 4(b). The narrow width guarantees higher contrast. One can expect that the narrow selection of an atomic cloud is useful for atomic interferometers because it demonstrates higher contrast. However, it decreases the number of detected atoms, as shown in Fig. 4(c). The black solid line in Fig. 4(c) indicates the calculated atom number. The reduction in the atom number degrades the short-term sensitivity. The short-term sensitivity, where only the shot noise for detecting the atom number is considered, is given by [18]

$$\Delta\Omega = \frac{1}{C(t_w)\sqrt{2N(t_w)}} \frac{1}{v_c k_{\text{eff}} T_R^2}. \tag{10}$$

Figure 4(d) shows the calculated short-term sensitivity (gray solid line) with $N = 1 \times 10^6$. The sensitivity of the fully integrated case is higher than that of the narrow selection case, based on our calculation. The enhancement in the contrast achieved by the narrow spatial selection is insufficient to overcome the reduction in the atom number.

In the experiment, we repeatedly recorded the atomic fraction change and the corresponding phase for 1000 s. The measured phases were converted to the angular velocities and the Allan deviation was calculated. The sensitivity as a function of the time gate width of an atomic cloud slice is plotted with circles, as shown in Fig. 4(d). We did not observe a significant difference between the narrow selection case and the full integration case.

Also the measured sensitivity [7.7×10^{-5} (rad/s)/$\sqrt{\text{Hz}}$] is not as good as the value calculated from Eq. (10) [2.0×10^{-6} (rad/s)/$\sqrt{\text{Hz}}$]. If the phase fluctuation sources that causes extra noise, such as Raman laser phase fluctuation, vibration, temperature changes, and atom trajectory variations were sufficiently suppressed, the effect of the sensitivity response on the time gate width of an atomic cloud slice would be observable. Among the phase fluctuation sources, vibrations can be estimated by comparing the measured sensitivities in the velocity sensitive and in the velocity insensitive Raman configuration. The measured sensitivity in the velocity insensitive configuration, which is the absence of the effect of vibrations, was 3.3×10^{-5} (rad/s)/$\sqrt{\text{Hz}}$. Therefore, the contribution of vibrations is expected to reach 7.0×10^{-5} (rad/s)/$\sqrt{\text{Hz}}$ in our experiment. Based on the above estimation, we conclude that vibrations mainly limit the sensitivity in our experiment.

The large size of the Raman beam and the small size of the atomic cloud enhance the short-term sensitivity. The large size of the Raman beam guarantees the small intensity gradient so that the gradient of the Rabi frequency is reduced (i.e., $B \to 0$). The small size of the atomic cloud promises the small variation of the Rabi frequency because the variation of the Rabi frequency in the atomic cloud results from multiplication of the gradient of the Rabi frequency and the size of the atomic cloud. As a result, the combination of the large size of the Raman beam and the small size of the atomic cloud reduces the inhomogeneity of the Rabi frequency. That causes an increment of the Raman transition efficiency which implies contrast enhancement. In Eq. (9), the contrast $C(t_w)$ is maximized in the limit that $\sigma/r_d \ll 1$. The maximum contrast leads to the enhanced short-term sensitivity, as described in Eq. (10). If the power of the Raman beam is enough, the large size of the Raman beam can be easily realized by using a beam expander. The small size of the atomic cloud can be achieved by an optical lattice trap where the beam waist is usually an order of subhundred μm or a magnetic trap. Optical lattice launching can be a solution for launching a small cold atomic cloud trapped by an optical lattice or a magnetic trap [19].

As mentioned before, we assumed in our analysis that the velocity and position are not coupled, so that spatial selection does not act as velocity selection. On the other hand, there is the position-velocity correlation limit, in that the size of the atomic cloud at detection is much larger than the initial size of the atomic cloud, i.e., $|v - v_c|t_f \gg \sigma_0$ [20]. In this limit, the spatial selection narrows the velocity distribution. It will increase the contrast in the system rotating at moderate angular speed by limiting $\Delta\phi_{\text{rot}}(\vec{v})$.

IV. CONCLUSION

We have developed a light-pulse atom interferometer with a single large Raman beam which propagates along the horizontal direction. By adjusting the Raman pulse timing, a $\pi/2$-π-$\pi/2$ Raman pulse sequence was implemented and the atomic Mach-Zehnder interference fringes were obtained. We spatially analyzed the interference with the help of thin probe beam-based time-of-flight measurements. After adopting the Raman beam intensity profile and the atomic cloud density profile, the variation in spatial contrast was analytically described. From the experiment and the calculation, we concluded that the spatial selection enhances the contrast of the interference at the expense of reduced short-term sensitivity.

ACKNOWLEDGMENTS

The authors thank the anonymous referee for valuable comments. This work was supported by a grant to Atom Optic Sensor Laboratory for National Defense funded by Defense Acquisition Program Administration, Agency for Defense Development, and Institute of Civil Military Technology Cooperation.

[1] J. B. Fixler, G. T. Foster, J. M. McGuirk, and M. A. Kasevich, Science **315**, 74 (2007).

[2] A. Wicht, J. M. Hensley, E. Sarajlic, and S. Chu, Phys. Scripta **T102**, 82 (2002).

[3] M. Cadoret, E. de Mirandes, P. Cladé, S. Guellati-Khélifa, C. Schwob, F. Nez, L. Julien, and F. Biraben, Phys. Rev. Lett. **101**, 230801 (2008).
[4] A. Peters, K. Y. Chung, and S. Chu, Metrologia **38**, 25 (2001).
[5] Q. Bodart, S. Merlet, N. Malossi, F. Pereira Dos Santos, P. Bouyer, and A. Landragin, Appl. Phys. Lett. **96**, 134101 (2010).
[6] Y. Bidel, O. Carraz, R. Charrière, M. Cadoret, N. Zahzam, and A. Bresson, Appl. Phys. Lett. **102**, 144107 (2013).
[7] T. L. Gustavson, P. Bouyer, and M. A. Kasevich, Phys. Rev. Lett. **78**, 2046 (1997).
[8] I. Dutta, D. Savoie, B. Fang, B. Venon, C. L. Garrido Alzar, R. Geiger, and A. Landragin, Phys. Rev. Lett. **116**, 183003 (2016).
[9] T. Müller, M. Gilowski, M. Zaiser, P. Berg, Ch. Schubert, T. Wendrich, W. Ertmer, and E. M. Rasel, Eur. Phys. J. D **53**, 273 (2009).
[10] A. V. Rakholia, H. J. McGuinness, and G. W. Biedermann, Phys. Rev. Appl. **2**, 054012 (2014).
[11] B. Canuel, F. Leduc, D. Holleville, A. Gauguet, J. Fils, A. Virdis, A. Clairon, N. Dimarcq, Ch. J. Bordé, A. Landragin, and P. Bouyer, Phys. Rev. Lett. **97**, 010402 (2006).
[12] H. Xue, Y. Feng, S. Chen, X. Wang, X. Yan, Z. Jiang, and Z. Zhou, J. Appl. Phys. **117**, 094901 (2015).
[13] A. Gauguet, B. Canuel, T. Lévèque, W. Chaibi, and A. Landragin, Phys. Rev. A **80**, 063604 (2009).
[14] J. Dalibard and C. Cohen-Tannoudji, J. Opt. Soc. Am. B **6**, 2023 (1989).
[15] S. H. Yim, S.-B. Lee, T. Y. Kown, and S. E. Park, Appl. Phys. B **115**, 491 (2014).
[16] P. Storey and C. Cohen-Tannoudji, J. Phys. II France **4**, 1999 (1994).
[17] G. W. Hoth, B. Pelle, S. Riedl, J. Kitching, and E. A. Donley, Appl. Phys. Lett. **109**, 071113 (2016).
[18] T. L. Gustavson, Ph.D thesis, Stanford University, 2000.
[19] T. Kovachy, P. Asenbaum, C. Overstree, C. A. Donnelly, S. M. Dickerson, A. Sugarbaker, J. M. Hogan, and M. A. Kasevich, Nature (London) **528**, 530 (2015).
[20] S. M. Dickerson, J. M. Hogan, A. Sugarbaker, D. M. S. Johnson, and M. A. Kasevich, Phys. Rev. Lett. **111**, 083001 (2013).